

Contents lists available at ScienceDirect

# International Journal of Solids and Structures

journal homepage: www.elsevier.com/locate/ijsolstr





# Multi-strain path deformation behavior of AA6016-T4: Experiments and crystal plasticity modeling

Rishabh Sharma <sup>a</sup>, Dane Sargeant <sup>c</sup>, Sowmya Daroju <sup>b</sup>, Marko Knezevic <sup>b</sup>, Michael P. Miles <sup>c</sup>, David T. Fullwood <sup>a</sup>

- <sup>a</sup> Department of Mechanical Engineering, Brigham Young University, Utah, USA
- <sup>b</sup> Department of Mechanical Engineering, University of New Hampshire, NH, USA
- <sup>c</sup> Manufacturing Engineering Department, Brigham Young University, Utah, USA

#### ARTICLE INFO

# Keywords: AA6016-T4 Elasto-plastic self-consistent model Backstress Multi-strain path HREBSD GND SSD

#### ABSTRACT

The development of backstresses that occur during a strain path change when forming sheet metal renders final part geometry prediction, after springback, difficult using conventional models. Most deformation models do not explicitly account for the influence of these stresses. A more recently developed elasto-plastic self-consistent (EPSC) model incorporates the backstresses to influence the activation of slip systems for more accurate simulations of the complex material response. The current study assesses the performance of the EPSC model for deformation response of AA6016-T4 via multiple biaxial, plane-strain, and uniaxial tension strain paths. The response to complex strain paths was examined by first pre-straining under uniaxial, biaxial, and plane-strain tension, then by loading in uniaxial tension. The EPSC model predictions closely matched experimental results. The model correctly predicted the highest yield stress and sharpest transition from elastic to plastic deformation for uniaxial tension after an initial uniaxial pre-strain. Lower yield stress for uniaxial tension after first pre-straining in biaxial and plane-strain tension is also correctly predicted, along with a smoother transition from elastic to plastic behavior. A linear geometrically necessary dislocation (GND) development, with strain, was observed using high-resolution electron backscattered diffraction (HREBSD) while a quadratic statistically stored dislocation (SSD) development was predicted by the model. The comparison revealed an expected transition from kinematic to isotropic hardening at higher strains. Finally, at higher strain levels the backstress accounted for around 15% of the total subsequent flow stress in all pre-strain cases.

# 1. Introduction

Backstresses that occur during plastic straining in most metals manifest in phenomena such as non-linear unloading, springback, and the Bauschinger effect (BE). These phenomena are typically more pronounced for a non-proportional strain path, leading to a final part geometry that is difficult to predict, after springback. Forming of complex geometries, such as channels in the automotive industry, is performed using non-monotonic deformation. Such geometries usually require multi-step forming to produce the final part for which a complete understanding of the strain path change behavior of the material is necessary. Graf highlights the change in formability levels for a given strain path via a forming limit diagram (FLD) for AA2008 (Graf and Hosford, 1993) and AA6111-T4 (Graf and Hosford, 1994). Lloyd et al. documented findings from tensile pre-strained samples, and subsequent orthogonal tensile loading for AA11100-0, AA3003-0, AA2036-0, and AA5182-0 (Lloyd and Sang, 1979). Laukonis et al. documented the hardening behavior of AA2036-T4 under uniaxial tension after a biaxial

pre-strain (Laukonis and Ghosh, 1978). This early work done by Lloyd et al., Graf et al., and Laukonis et al. develops understanding between the strain path change and mechanical response of the Al alloys but generally does not explicitly include the role of backstress development. Finite element (FE) models can be employed to simulate a metal's response to deformation, including strain path changes. However, most plasticity models do not explicitly account for the generation and influence of backstresses. In a recent study, Chen et al. observed and modeled the hardening behavior of AA2A12-T4, AA5052-H32, AA6061-T6, and AA7075-T651 under uniaxial and forward-reverse shear loading (Chen et al., 2019). Their Visco-Plastic Self Consistent (VPSC) model's hardening law incorporated necessary backstress development to predict macroscopic mechanical response and texture evolution. However, VPSC does not consider elastic deformation and, as a result, does not calculate inter-granular sources of backstress. Therefore, a need to understand the microstructure evolution and the characteristic work hardening behavior upon strain path change using elastoplasticity is apparent.

The current paper assesses the performance of an elasto-plastic self-consistent (EPSC) model, with backstress effects incorporated, for multi-strain-path deformation in AA6016-T4. The yield behavior and subsequent hardening during uniaxial tension following biaxial, plane-strain, and uniaxial tension pre-straining are modeled and compared with the experimental results. The backstress contribution to the overall flow stress is analyzed. Digital image correlation (DIC) was employed to calculate the effective strains under biaxial and plane-strain pre-straining of the alloy. Dislocation density evolution is observed in terms of GNDs in the experimental results and compared with the predicted statistically stored dislocation (SSD) density.

In precipitation-hardened aluminum alloys, backstress development is associated with the evolution of dislocation substructures influenced by Orowan looping around the precipitates, grain boundary pileups, and cell structures (El-Madhoun et al., 2003; Moan and Embury, 1979; Stoltz and Pelloux, 1974, 1976). The development of these substructures causes dislocation heterogeneities in the microstructure which accommodate strain gradients. Backstresses accumulate in these strain gradient regions, due to the cumulative effect of multiple dislocations of the same polarity. The backstresses naturally oppose the applied resolved shear stress, contributing to the hardening behavior. However, upon reversal or strain path change, previously accumulated backstress may assist the movement of dislocations, resulting in non-linear unloading and softening and/or lower subsequent yield stresses. Taylor-type and mean-field self-consistent models do not traditionally account for the heterogeneities in the micromechanical fields that develop across the sample, or the associated complex backstress behavior – particularly due to strain path change (Al-Harbi et al., 2010; Knezevic et al., 2008, 2009; Taylor, 1938).

Models developed in the last couple of decades started incorporating backstresses into their hardening law. Chen et al. include an incremental deviatoric backstress tensor in their ratcheting simulations under a biaxial strain path (Chen et al., 2003). Goh et al. assumed backstress to follow a pure kinematic hardening rule to simulate and understand the effect of crystallographic orientation of the grains on plastic deformation under fretting conditions (Goh et al., 2003). Li et al. predict transient hardening after strain path change from biaxial to uniaxial tension (Li et al., 2003). Their FEA model associates backstresses with kinematic hardening to solve the problem of plastic anisotropy induced by both texture and strain-path change.

Computationally intensive crystal plasticity finite element (CPFE) and crystal plasticity fast Fourier transform (CPFFT) models can predict the micromechanical fields at the grain level (Liu et al., 2010; Raabe and Roters, 2004; Rovinelli et al., 2020), potentially simulating the deformation of an entire representative volume element (Eghtesad et al., 2018; Knezevic and Savage, 2014; Savage and Knezevic, 2015). However, texture-level mean-field self-consistent models such as EPSC are more computationally efficient – particularly for complex strain paths. These models have proven effective in predicting the homogenized flow stress and texture evolution of polycrystals. In particular, studies have shown that the EPSC models are capable of predicting microstructural response to strain path change such as residual stress fields, elastic lattice strains, non-linear unloading, the Bauschinger effect, hardening rates, and overall texture of the material (Neil et al., 2010; Nugmanov et al., 2018; Wollmershauser et al., 2012; Zecevic et al., 2015, 2016, 2019). In this paper, an EPSC model that incorporates a phenomenological backstress law along with a dislocation density-based hardening law is used to study the deformation response of AA6016-T4. Previously, it was found to accurately model reverse loading and simple loading deformation in AA6022-T4 (Barrett and Knezevic, 2019; Zecevic and

Knezevic, 2019).

# 2. Experimental procedures

The composition of the AA6016–T4 alloy is given in Table 1. The material was provided by Commonwealth Aluminum. The forming limits of the material were first measured under proportional uniaxial, biaxial, and plane-strain tension. The tensile specimens were machined along the rolling direction (RD), transverse direction (TD), and  $45^\circ$  to RD of the sheet according to the ASTM E8 sample configuration shown in Fig. 1. The specimens were pulled at a 1.5 mm/min crosshead displacement rate and the force-strain data were recorded using a load cell and extensometer. The specimens' thickness and width were recorded at five different points along the gauge length to accurately calculate applied true stress to evaluate it against the strain data from the extensometer.

An Interlaken Hydraulic press was used for plane-strain and biaxial tension forming experiments, using standard Marciniak tooling, including a 100 mm diameter flat-topped punch. The press has a maximum clamp load capacity of 334 kN and a maximum punch load of 223kN. The clamping system included small lock beads to restrain the blanks. All loading experiments were performed with a clamp load of 200 kN, using 0.5 mm thick Teflon sheets between the sheet and punch, and mineral oil between the punch, Teflon sheet, carrier blank, and sheet specimen. Biaxial and plane-strain tension paths were achieved by varying the dimensions of the sheet specimens as specified in Figs. 2 and 3.

The biaxial and plane-strain tension tests were guided by a previous study on DP600 steel sheets by Cheng et al. (2017). Marciniak tooling was used because the punch geometry enables different levels of strain to be imparted to a sheet blank with a large flat section, unlike limiting dome height tooling. As is often done in Marciniak testing, a carrier blank, of the same material and thickness as the sheet specimen, was introduced between the specimen and the punch to better distribute strain and to prevent pre-mature localization in the sheet specimen (Fig. 3). After pre-straining biaxial and plane-strain tension samples to several different levels, scaled-down ASTM E8 tensile specimens were cut from the flat portion of the blank for subsequent uniaxial tension straining. This allowed for evaluating the effect of a strain path change (biaxial  $\rightarrow$  uniaxial tension, plane-strain  $\rightarrow$  uniaxial tension). In the current study, these specimens are referred to as 'pre-strained specimens. The experimental Marciniak forming setup could be controlled either by an applied force or forming distance as user input. The specimens were taken to failure under a given strain path, and then subsequent trials were taken to a forming distance that was a given percentage of the failure strain. The pre-strained specimens were cut from sheets that were strained to 25%, 50%, 75%, and 95% of the effective failure strain of the material for each strain path. The actual strain in the sheet was obtained from digital image correlation (DIC).

A 2D real-time deformation strain pattern of the deforming surface of



Fig. 1. ASTM E8 uniaxial tension specimen and dimensions in millimeters.

**Table 1**Nominal chemical composition of AA 6016-T4.

Sample	Al	Si	Mg	Fe	Mn	Zn	Cu	Ti	Cr
Al 6016	96.4–98.8	1.0-1.5	0.25-0.6	0-0.5	0-0.2	0-0.2	0-0.2	0-0.15	0-0.1

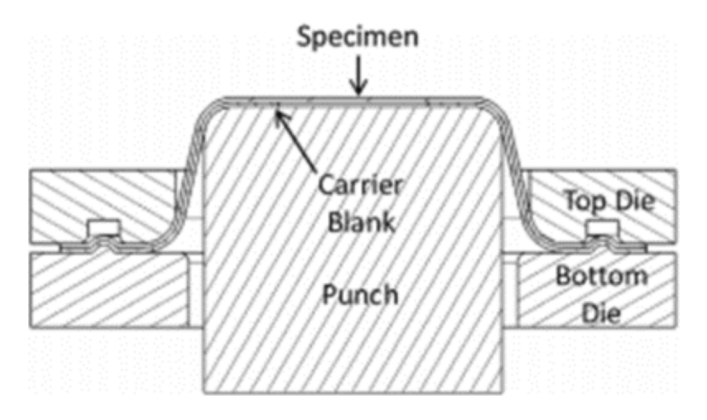
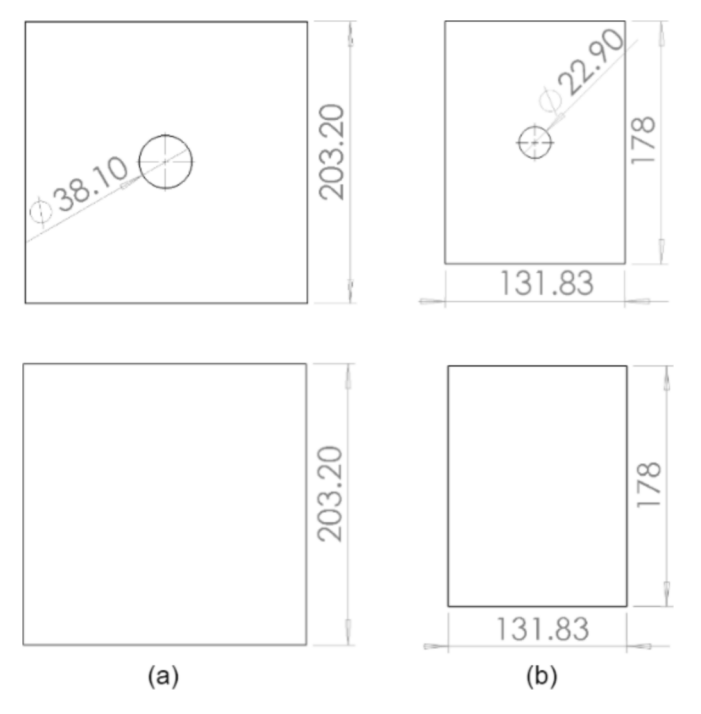


Fig. 2. Marciniak tooling for biaxial tension and plane-strain tension testing (Cheng et al., 2017).



**Fig. 3.** Dimensions of (a) biaxial and (b) plane-strain tension (top) carrier blanks and (bottom) sheet specimens.

each sheet specimen was obtained by performing DIC using an Aramis system from Trilion Quality Systems (ARAMIS 3D Digital Image Correlation Strain 3D Deformation, 2011). The surface strains were calculated using the Aramis software as shown in Fig. 4.

DIC measurements of the specimen surface during Marciniak testing allowed for strain path validation of the biaxial and plane-strain tension tests. The strain values plotted for the biaxial and plane-strain experiments were calculated by averaging a series of points in a line across the middle of the DIC strain map (highlighted in red, as seen in Fig. 4). Examples of plots used to validate strain path are shown for biaxial tension (Fig. 5a) and plane-strain tension (Fig. 5b). The biaxial tension experiment produced an almost perfectly proportional biaxial tension strain path during the test, while the plane-strain tension experiments show very slight positive minor strains during most of the test.

A small sample sectioned from the gauge length of the pre-strained specimens was prepared for the microstructural analysis. The microscopy samples were removed using a diamond blade cutter, to avoid further deformation of the material, and mounted in epoxy resin to polish for EBSD scanning. The ND surface of the samples was first ground with grits of 400, 600, 800, 1200, and 1200 fine abrasive paper. The ground samples were then electropolished using an electrolyte solution of 1:9 ratio of perchloric acid and methanol under 20 V and 2 amps at room temperature for 30 s. The polished samples were then milled in an inert Argon gas environment of JEOL ion-beam cross-section polisher to remove the initial strain layer induced by polishing. The surface was first coarsely milled at 5 kV and 4.2 atm for 20 mins. A second finer step removed unevenness by milling the surface at 4 kV and 6.2 atm for 5 mins. The polished surface of the samples was scanned using EDAX OIM software (OIM 6.0, 2010), and patterns were saved for evaluation using high-resolution EBSD (HREBSD).

The initial (unstrained material) texture was measured using EBSD. Also, uniaxial, biaxial, and plane-strain tension specimens were all evaluated for GNDs, as a function of strain to compare against the dislocation density calculated by the model. HREBSD was employed to compute the GND density in the base material and the strained specimens, using OPENXY (2015; Ruggles and Fullwood, 2013). Three different areas of  $120 \times 120$  microns with 70 nm step size were scanned for GND content on each specimen as illustrated in Fig. 6.

Scaled-down ASTM E8 tensile specimens were waterjet cut from the pre-strained biaxial and plane-strain specimens. The pre-strained specimens were then tested under uniaxial tension to determine their residual ductility and work hardening behavior.

# 2.1. EPSC model

The EPSC polycrystal model used in this study was first applied by

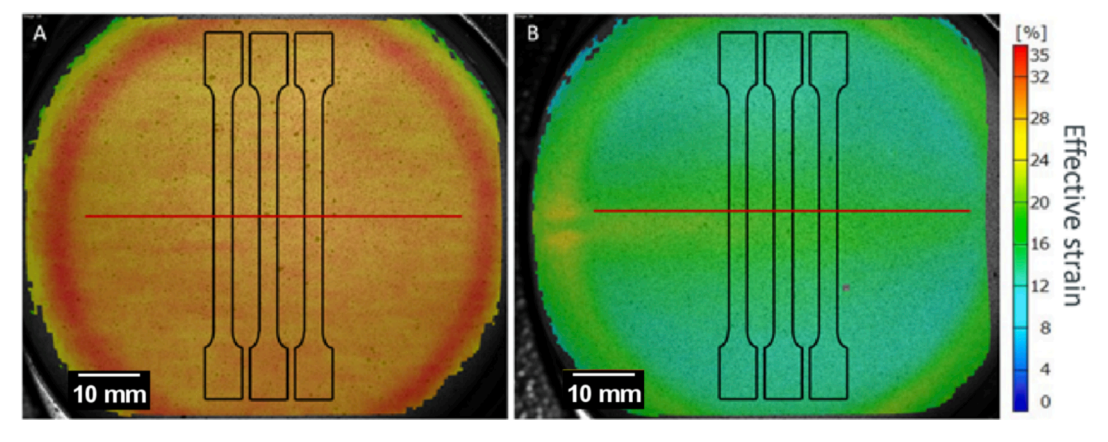


Fig. 4. DIC strain patterns (percent major strain) for biaxial tension at 75% of failure (left), and plane-strain tension at 95% of failure (right). After imparting different levels of pre-strain to these sheet blanks, tensile specimens were cut, as shown, and then tested in-situ in the SEM. The size of the dogbones is illustrative, and not to scale.

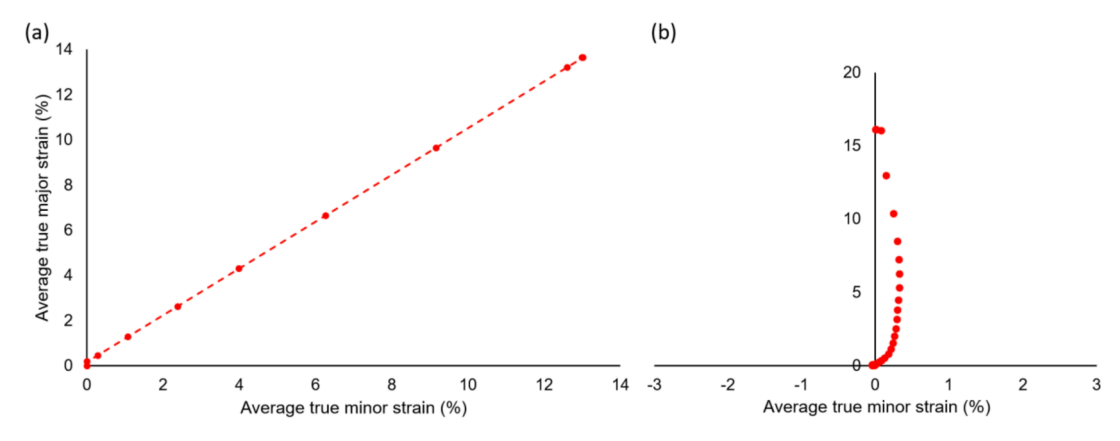
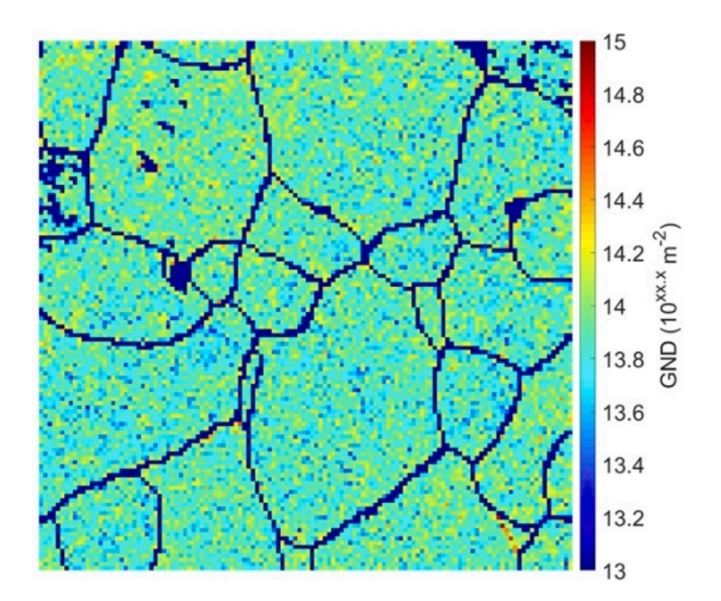


Fig. 5. Strain paths from DIC measurements for (a) biaxial and (b) plane-strain tension.



**Fig. 6.** GND map produced from HREBSD measurements for unstrained AA6016-T4.

Zecevic and Knezevic (2019) to predict cyclic strains in AA6022-T4. The current study used the same approach for modeling and interpreting the experimental mechanical data under multi-strain path deformation for AA6016-T4. The relation of Jaumann stress rate,  $\hat{\sigma}$ , and strain rate,  $\dot{\epsilon}$ , is used in EPSC for a material point, whether a single crystal or a polycrystalline aggregate (Nagtegaal and Veldpaus, 1984; Neil et al., 2010).

$$\widehat{\boldsymbol{\sigma}} = L\dot{\boldsymbol{\varepsilon}} = \dot{\boldsymbol{\sigma}} + \boldsymbol{\sigma}W - W\boldsymbol{\sigma} \tag{1}$$

The tensorial quantities,  $\sigma$ , W, and L are the Cauchy stress, spin, and tangent stiffness, respectively. These quantities at the crystalline level are denoted with a superscript, c as  $\sigma^c$ ,  $W^c$ , and  $L^c$ . In the description that follows, a dot product and a tensor product will be denoted with  $\cdot$  and  $\otimes$ , respectively. Tensors are denoted by bold letters, while scalars are not bold. Hooke's law is used at the crystal level.

$$\widehat{\boldsymbol{\sigma}}^{c} = \boldsymbol{L}^{c} \dot{\boldsymbol{\varepsilon}}^{c} = \boldsymbol{C}^{c} \left( \dot{\boldsymbol{\varepsilon}}^{c} - \dot{\boldsymbol{\varepsilon}}^{pl,c} \right) - \boldsymbol{\sigma}^{c} tr(\dot{\boldsymbol{\varepsilon}}^{c})$$
(2)

where  $C^c$  and  $\dot{\epsilon}^{pl,c}$  are the elastic stiffness tensor and the plastic strain rate per crystal c, respectively. The latter is given by

$$\dot{\mathbf{c}}^{pl,c} = \sum_{s} \mathbf{m}^{s} \dot{\gamma}^{s} \tag{3}$$

where  $m^s = \frac{1}{2}(b^s \otimes n^s + n^s \otimes b^s)$  is the Schmid tensor and  $\dot{\gamma}^s$  is the shear strain.

The Schmid tensor is defined by the slip system geometry, in which  $b^s$  is the Burger's vector and  $n^s$  is the slip system normal. Starting from the crystal volume average  $\hat{\sigma} = \langle \hat{\sigma}^c \rangle$  and  $\dot{\varepsilon} = \langle \dot{\varepsilon}^c \rangle$ , the polycrystalline L can be evaluated using the standard self-consistent homogenization procedure (Eshelby, 1957; Lipinski and Berveiller, 1989; Neil et al., 2010; Turner and Tomé, 1994). The particular version of the model used in the present work is from (Zecevic and Knezevic, 2019).

The index, s, spans over available slip systems in a grain c. The model incorporates a strain-path sensitive dislocation density-based law for the evolution of slip system resistance,  $\tau_c^s$ , and a slip system level back-stress law to influence the resolved shear stress for activation. These laws along with latent hardening are aimed at predicting the anisotropic mechanical response of the alloy during monotonic loading as well as the particularities pertaining to the load reversal deformation such as non-linear unloading, the BE, and changes in the hardening rates. Since elasto-plastic, the model approximates the inter-granular stresses using self-consistent homogenization. Activation per slip system is determined using the two conditions.

$$\boldsymbol{\sigma}^c \bullet \boldsymbol{m}^s - \boldsymbol{\tau}^s_{bs} = \boldsymbol{\tau}^s_c \tag{4}$$

$$\widehat{\boldsymbol{\sigma}}^c \bullet \boldsymbol{m}^s - \dot{\boldsymbol{\tau}}^s_{bs} = \dot{\boldsymbol{\tau}}^s_c \tag{5}$$

where,  $\tau_{bs}^*$  is a slip system back-stress governing the kinematic hardening effects (Wollmershauser et al., 2012). Condition (4) implies that the stress state is on the crystal yield surface. Condition (5) implies consistency providing that the stress state stays on the crystal yield surface (Knockaert et al., 2000); Milovan (Zecevic et al., 2019). The slip system resistance and back-stress evolve using

$$\dot{\tau}_c^s = \sum_i h^{ss'} \dot{\gamma}^{s'} \tag{6}$$

$$\dot{\tau}_{bs}^{s} = \sum_{i} h_{bs}^{ss} \dot{\gamma}^{s} \tag{7}$$

where  $h^{ss}$  and  $h^{ss}_{bs}$  are a hardening matrix consisting of partial derivatives,  $h^{ss} = \frac{\partial r^s_b}{\partial r^s}$ , and a back-stress matrix consisting of partial derivatives,  $h^{ss}_{bs} = \frac{\partial r^s_b}{\partial r^s}$ . Next, we summarize the slip resistance and the back-stress laws for defining these partial derivatives.

In the description that follows, s+ and s- are used to define a positive and a negative slip direction for every s belonging to a slip family (mode) $\alpha$ . Resistance to slip consists of three terms.

$$\tau_c^s = \tau_0 + \tau_{forest}^s + \tau_{debris} \tag{8}$$

with  $\tau_0$  denoting an initial dislocation free fixed value of slip resistance (Peierls stress), while  $\tau_{forest}^s$  and  $\tau_{debris}$  are evolving terms with statistically stored forest dislocations and debris dislocations, respectively. These

two terms are defined as

$$\tau_{forest}^{s} = b\chi G \sqrt{\sum_{s'} L^{ss'} \rho_{tot}^{s'}}$$
 (9)

$$\tau_{debris} = 0.086Gb\sqrt{\rho_{deb}}log\left(\frac{1}{b\sqrt{\rho_{deb}}}\right)$$
 (10)

In the above equations, b is the Burgers vector magnitude ( $b=2.8610^{-10} \mathrm{m}$  for Al),  $\chi$  is an interaction constant (Lavrentev, 1980; Mecking and Kocks, 1981) ( $\chi=0.9$ ),  $\rho_{tot}^s$  is the total density of forest dislocation for the  $s^{th}$  slip system,  $\rho_{deb}$  is the density of debris dislocation population, G(26GPa) is the shear modulus, and  $L^{ss}$  is a latent hardening interaction matrix.

The total density of forest dislocations consists of.

$$\rho_{tot}^{s} = \rho_{for}^{s} + \rho_{rev}^{s^{+}} + \rho_{rev}^{s^{-}} \tag{11}$$

where  $\rho_{for}^s$  is the forward and  $\rho_{rev}^{s^+}$  and  $\rho_{rev}^{s^-}$  are the reversible densities of dislocations associated with the  $s^+$  and  $s^-$  system directions. These densities of dislocations evolve with shearing as follows (Kitayama et al., 2013; Zecevic and Knezevic, 2019)

(If  $d\gamma^{s^{+}} > 0$ ).

$$\frac{\partial \rho_{for}^s}{\partial \gamma^s} = (1 - p)k_1 \sqrt{\sum_{s'} g^{ss'} \rho_{tot}^{s'}} - k_2(\dot{\varepsilon}, T) \rho_{for}^s$$
(12)

$$\frac{\partial \rho_{rev}^{s^+}}{\partial \gamma^s} = p k_1 \sqrt{\sum_{s'} g^{ss'} \rho_{tot}^{s'}} - k_2(\dot{\varepsilon}, T) \rho_{rev}^{s^+}$$
(13)

$$\frac{\partial \rho_{rev}^{s^{-}}}{\partial y^{s}} = -k_{1} \sqrt{\sum_{s'} g^{ss'} \rho_{tot}^{s'} \left(\frac{\rho_{rev}^{s}}{\rho_{0}^{s}}\right)^{m}}$$
(14)

(If  $d\gamma^{s^-} > 0$ ).

$$\frac{\partial \rho_{for}^s}{\partial \gamma^s} = (1 - p)k_1 \sqrt{\sum_{s'} g^{ss'} \rho_{tot}^{s'}} - k_2(\dot{\varepsilon}, T)\rho_{for}^s$$
(15)

$$\frac{\partial \rho_{rev}^{s^+}}{\partial \gamma^s} = -k_1 \sqrt{\sum_{s^*} g^{ss^*} \rho_{tot}^{s^-}} \left( \frac{\rho_{rev}^{s^+}}{\rho_0^s} \right)^m \tag{16}$$

$$\frac{\partial \rho_{rev}^{s^{-}}}{\partial \gamma^{s}} = pk_1 \sqrt{\sum_{s'} g^{ss'} \rho_{tot}^{s'}} - k_2(\dot{\varepsilon}, T) \rho_{rev}^{s^{-}}$$
(17)

with  $\rho_{for}^s(\gamma^s=0)=3.9\mathrm{e}10^{12}m^{-2}$ ,  $\rho_{rev}^{s^+}(\gamma^s=0)=0$  and  $\rho_{rev}^{s^-}(\gamma^s=0)=0$ . In the above expressions,  $k_1$  is a fitting parameter controlling the rate of dislocation generation, while  $k_2$  is calculated as a rate-sensitive term controlling dynamic recovery of dislocations (Beyerlein and Tomé, 2008); p is a reversibility parameter in the range from 0 to 1 (taken as 0.2),  $g^{ss^-}$  is another interaction matrix taken as a full of 1.0 (Khadyko et al., 2016; Kocks et al., 1991; Teodosiu and Raphanel, 1991); m is a parameter controlling the rate of recombination of dislocations (the value is set to 0.5 (Wen et al., 2015), and  $\rho_0^s$  is the total density of dislocation at the local path reversal on the system,  $s^{th}$  (Kitayama et al., 2013).

The rate-sensitive term,  $k_2$ , is calculated using.

$$\frac{k_2}{k_1} = \frac{\chi b}{g} \left( 1 - \frac{k_B T}{D b^3} ln \left( \frac{\dot{\varepsilon}}{\dot{\varepsilon}_0} \right) \right) \tag{18}$$

with the Boltzmann constant,  $k_B$ , a reference strain rate,  $\dot{\varepsilon}_0 = 10^7$ , drag stress,D, and an effective activation enthalpy, g. The debris density of dislocation is incremented using

$$\sum_{s} \frac{\partial \rho_{deb}}{\partial \gamma^{s}} = \sum_{s} qb \sqrt{\rho_{deb}} k_{2}(\dot{\epsilon}, T) \rho_{tot}^{s}$$
(19)

with a fitting parameter for the rate of dislocation recovery, q.

Next, we turn our attention to a back-stress law for defining the back-stress matrix,  $h_{\rm bs}^{\rm ss}$ . In general, backstress has intra-granular and intergranular sources in polycrystals. Inter-granular sources are the interactions between individual grains of different crystal orientations. As already mentioned, these effects are approximated in the EPSC formulation because every grain interacts with the averaged polycrystalline response unlike in CPFE or CPFFT where grain-to-grain interaction can be explicitly modeled. Intra-granular sources such as any incompatibilities between hard and soft regions within grains are modeled by the phenomenological law as follows (Zecevic and Knezevic, 2019).

$$\boldsymbol{\tau}_{bs}^{s} = \boldsymbol{m}^{s} \bullet \boldsymbol{\sigma}_{bs}^{c} = \boldsymbol{\tau}_{bs,sys}^{s} + 2 \sum_{i} \boldsymbol{m}^{s} \bullet \boldsymbol{m}^{s} \boldsymbol{\tau}_{bs,sys}^{s}$$
 (20)

where

$$\tau_{bs,sys^*}^{s'} = \begin{cases} \tau_{bs,sys}^{s'} i f \tau_{bs,sys}^{s'} > 0\\ 0 i f \tau_{bs,sys}^{s'} < 0 \end{cases}$$
 (21)

In the above equations,  $\sigma_{bs}^c$  is the back-stress tensor based on the contribution from the slip system level sources over s when  $s \neq s$ .

The slip system level back-stress is

(if 
$$d\gamma^{s^+} > 0$$
 and  $\tau_{bs,sys}^{s^+} > 0$ ).

$$\tau_{b_{x,yy_{s}}}^{s^{+}} = \tau_{b_{s}}^{sat} (1 - exp(-\nu \gamma^{s^{+}}))$$
(22)

$$\tau_{b_{x,\text{nw}}}^{s^-} = -A \tau_{b_{x,\text{nw}}}^{s^+} \tag{23}$$

(if 
$$d\gamma^{s^+} > 0$$
 and  $\tau^{s^+}_{bs,sys} < 0$ ).

$$\tau_{bs,sys}^{s^{+}} = -(A+1)\tau_{bs}^{sat} exp\left(-\frac{\gamma^{s^{-}}}{\gamma_{b}}\right) + \tau_{bs}^{sat}$$
(24)

$$\tau_{bs,sys}^{s^{-}} = -\frac{1}{A}\tau_{bs,sys}^{s^{+}} \tag{25}$$

The fitting constants for the back-stress law are a saturation value,  $\tau_{bs}^{sat}$ , a parameter governing an asymmetric evolution in s+ and s-, A, the denominator,  $\gamma_b$ , and a multiplier,  $\nu$ . The shearing strain,  $\gamma^s$ , is a value at the load reversal. Note that  $\tau_{bs}^{c^+}$  opposes the driving force in  $s^+$ :  $m^{c,s+} \bullet \widehat{\sigma}^c - \tau_{bs}^{c,s+} = \tau_c^{c,s}$ , which means that  $\tau_{bs}^{c,s+}$  reduces the driving force. In contrast,  $\tau_{bs}^{c,s-}$  aids the driving force in  $s^-$ :  $m^{c,s-} \bullet \widehat{\sigma}^c - \tau_{bs}^{c,s-} = \tau_c^{c,s}$ .

# 3. Results and discussion

The initial material characterization was performed under uniaxial tension as a baseline for subsequent strain path change tests. The model was calibrated for AA6016-T4 using the initial texture and the hardening parameters were calibrated by fitting the model to the measured uniaxial tensile stress–strain curve in RD (discussed later in this section). Minor differences were observed in the deformation response for RD, TD, 45° to RD (Table 2). The strain-to-failure measured for the three

**Table 2**Mechanical properties of AA6016-T4 under uniaxial tension true stress–strain curves

Sample orientation	Young's modulus (GPa)	Strain-to- failure	Yield strength (MPa)	Ultimate tensile strength (MPa)
RD	70.5	0.27	142	344
45° to RD TD	70.8 71.7	0.245 0.249	140 140	321 326

orientations ranges from 0.24 to 0.27, with RD being the greatest.

The latent hardening interaction matrix,  $L^{ss'}$  (Eq. (9)), was established in the earlier work involving AA6022-T4 (Zecevic and Knezevic, 2018). The actual values for the latent hardening coefficients were calculated for FCC metals by Hoc and Devincre employing dislocation dynamic simulations. The same values were successfully used for several FCC metals (Devincre et al., 2006; Ghorbanpour et al., 2017; Hoc et al., 2004). The same values are used for AA6016-T4 and are listed in Table 3. The six types of dislocation interactions represented by the matrix are (1)  $a_0$ : self-interaction between dislocations belonging to the same slip system, (2)  $a_1$ : coplanar-interaction between dislocations on the same slip plane, (3)  $a_2$ : interaction resulting in Hirth lock, (4)  $a_3$ : collinear interaction between dislocations on cross slip planes, (5) a<sub>4</sub>: interaction resulting in sessile Lomer-Cottrell locks, and (6)  $a_5$ : glissile lock. The rest of the fitted hardening law and backstress parameters calibrated using monotonic data are given in Tables 4 and 5, respectively. The initial values of the parameters, taken to be the starting points of the calibration process, were retained from the earlier study involving AA6022-T4 (Zecevic and Knezevic, 2019). The parameters identified for the alloy are the initial resistance to slip,  $\tau_0$ , trapping rate coefficient,  $k_1$ , drag stress, D and activation barrier for de-pinning, g. The identification procedure started by varying  $\tau_0$  to reproduce onset in yielding. Next,  $k_1$ , was varied such that the initial hardening slopes are captured. Next, g and D are varied to match the latter hardening rates. Finally, q was fit to capture the later stage in the hardening rates. Concurrently with the hardening parameters, the backstress law parameters were identified.

The EPSC model requires an estimate of initial dislocation density. During the calibration exercise, the value per slip system in Table 4 (4.68e13 m<sup>-2</sup> summed over the 12 slip systems) was deemed to be consistent with a well-annealed material, as per the manufacturer's advice. Subsequently, this value was compared against HREBSD measured values of GND content (that was not initially available) and previously published dislocation content data for other aluminum alloys, as listed in Table 6. Note that the EPSC model does not distinguish between SSDs and GNDs; all the dislocations due to plastic straining are assumed to be SSDs. Furthermore, measured GND content will always be lower than total dislocation content, which is the sum of GNDs and SSDs. The estimated dislocation content used in the model is slightly lower than the HREBSD measured GND value. It is approximately an order of magnitude lower than the x-ray diffraction (XRD) measured total dislocation content of AA6061-T6 (Woo et al., 2010) and AA2024-T6 (Mirzaei et al., 2015). However, lower GND density was measured in solution-treated AA6082 via EBSD (Zheng et al., 2021). Therefore, it appears that the initial calibrated estimate from the EPSC model is within reasonable tolerances.

The EPSC predictions for the measured uniaxial tests, following the calibration exercise, are shown in Fig. 7. The slight anisotropy in the mechanical properties is captured well by the EPSC model, indicating that the effect of texture is appropriately taken into account. All subsequent uniaxial tests were measured and predicted in the RD orientation of the sheet in the remainder of this study. It should be noted that while the model is able to match the measured work hardening trends for all three orientations it is unable to predict the onset of plastic instability. Plastic instability is triggered when the ductility of the material is exhausted, and further plastic strains are accommodated by non-uniform deformation at the sites containing micro-defects such as microvoids. This leads to strain localization and failure soon after. Therefore, only uniform elastic and plastic strains are compared.

During the pre-strain experiments, a higher forming limit was

**Table 3**Latent hardening coefficients.

$a_0$	$a_1$	$a_2$	$a_3$	$a_4$	$a_5$
0.068	0.068	0.0454	0.625	0.137	0.122

Table 4 Fitting parameters used for the evolution of slip resistance for  $111\langle11^-0\rangle$  slip mode in AA6016-T4.

$\tau_0[\mathrm{MPa}]$	$k_1[m^{-1}]$	g	D[MPa]	$\rho_{for}^{s} \big[ m^{-2} \big]$
25	1.38 x10 <sup>8</sup>	0.09	400	4.68e13

**Table 5**Fitting parameters used for the evolution of slip system kinematic backstress for AA6016.T4

$ au_{bs}^{sat}$ [MPa]	ν	$\gamma_b$	Α
5	560	0.001	1

**Table 6**Comparison of dislocation densities.

Material	Measurement method	Dislocation density $(m^{-2})$
AA6016-T4	EPSC estimate	4.68e13
	HREBSD GND	8.2e13
AA6061-T6	XRD(Woo et al., 2010)	4.5e14
AA2024-T6	XRD(Mirzaei et al., 2015)	9e14
Solution treated AA6082	Mtrex GND(Zheng et al., 2021)	9.7e12

measured for biaxial compared to plane-strain and uniaxial tension, before localization. Biaxial tension resulted in the highest effective strain at 0.42 compared to 0.18 for plane-strain and 0.25 for uniaxial tension measured using DIC. This is consistent with published data; in FCC metals biaxial tension deformation is found to activate a relatively higher number of slip systems, which leads to a more homogeneous stress state in comparison to plane-strain and uniaxial tension (Dequiedt et al., 2015; Segurado and LLorca, J, 2010).

During plastic deformation, the dislocation density of the material increases due to dislocation generation from various sources such as shear of the lattice structure, multiplication from Frank-read sources and pinning around the precipitates, etc. This requires an increase in flow stress for further deformation which manifests as work hardening. The overall dislocation density of the material is given by the sum of SSDs and GNDs. SSDs are the accumulated dislocations caused by the mutual trapping in the crystal due to dislocation—dislocation interaction. They are in contrast to GNDs, which are accumulated in strain gradient fields caused due to the geometric constraints of the crystal lattice.

The development of GND from HREBSD is compared to SSD calculations from EPSC for pre-strain deformations under all three strain paths in Fig. 8. HREBSD indicates an approximately linear GND increase for all pre-strain paths, in line with studies on correlations between plastic strain and kernel average misorientation (KAM) (Brewer et al., 2009; Wright et al., 2016). KAM is a measure of local grain misorientations from EBSD that is known to correlate with GND content. On the other hand, EPSC predicts a quadratic increase in SSDs. While the EPSC-predicted dislocation density only incorporates SSDs development as total (EPSC assumes no GNDs), some studies have found correlations between the densities of the two dislocation types. According to Ashby's theory of work hardening, while SSDs dominate the homogeneous deformation in the single crystals, the inhomogeneous deformation in polycrystals is dominated by GNDs (Jiang et al., 2013). Furthermore, GND development during plastic deformation is associated with kinematic hardening, dominating early hardening behavior, while SSDs multiply faster during later isotropic hardening (see Fig. 8 in (Ashby, 1970), and (Bouaziz et al., 2021; Ebobisse and Neff, 2010). Hence the measured and predicted trends in Fig. 8 generally follow expected trends.

The EPSC predictions for biaxial-to-uniaxial and plane-strain-to-

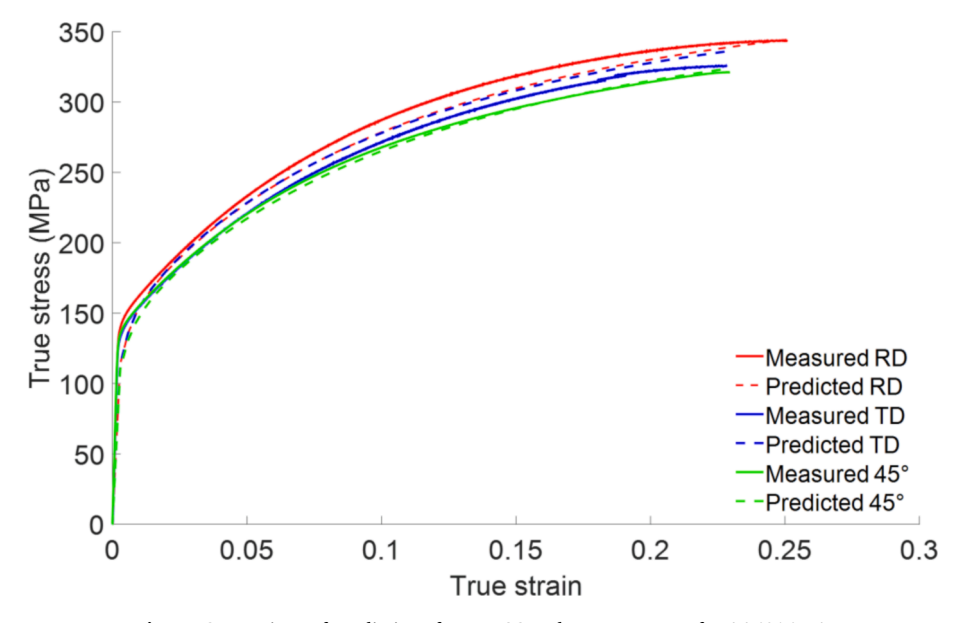
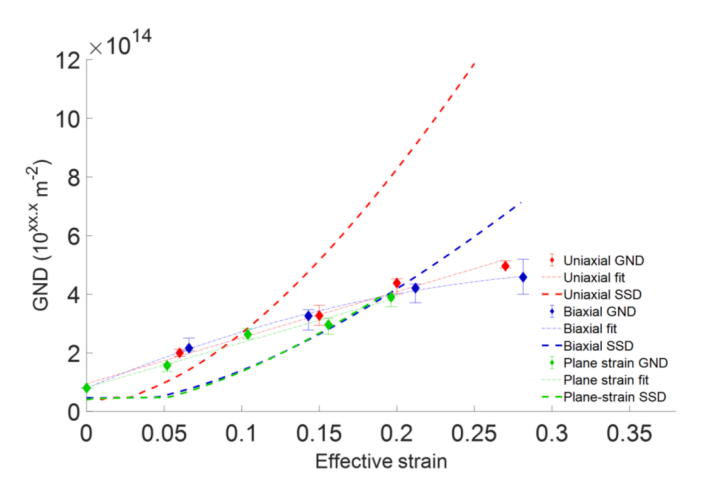


Fig. 7. Comparison of predictions from EPSC and measurements for AA6016-T4.



**Fig. 8.** GND development by HREBSD compared to SSD calculations by EPSC under uniaxial, biaxial, and plane-strain tension pre-strain deformation.

uniaxial tension pulls are compared to the experimental measurements in Fig. 9. Higher-strength levels are achieved for biaxial-to-uniaxial than plane-strain-to-uniaxial tension in both cases. Also, biaxial-to-uniaxial deformation generates a slightly more ductile response which is in-line with a previously published study for strain path change in AA6111-T4 (Graf and Hosford, 1994). The EPSC model is able to capture the

hardening behavior following a strain-path change with a slight overprediction of hardening rate for higher pre-strain levels, owing to signs of localization under biaxial and plane-strain tension at the higher pre-strains (Fig. 4). This indicates that some amount of damage was accumulated in the pre-strained specimens that produced a softer than predicted hardening response under subsequent uniaxial tension deformation.

The pre-strain levels for each strain path were selected as a percentage of final failure for that particular path, and hence the effective strains are not the same for each one. However, experiments with similar effective pre-strain levels (within 1.6%) were selected for a more detailed comparison of uniaxial tension ductility after pre-strain and compared to the EPSC predictions (Fig. 10). The yield strength of the pre-strained samples under uniaxial tension is in the increasing order of plane-strain, biaxial and uniaxial tension, as is well captured in EPSC simulations (Fig. 10). Furthermore, a sharp elasto-plastic transition can be observed for uniaxial-to-uniaxial deformation, followed by approximately linear hardening. However, a slower elasto-plastic transition for biaxial-to-uniaxial and plane-strain-to-uniaxial tension is demonstrated in observed and predicted curves. The reason for the higher strength level occurring in the uniaxial-to-uniaxial specimens, along with the sharp elasto-plastic transition and subsequent linear hardening, is postulated to be due to the increase in dislocation density on already activated slip systems from pre-straining, and an absence of dislocation recombination. Dislocation recombination is more likely under a strainpath change.

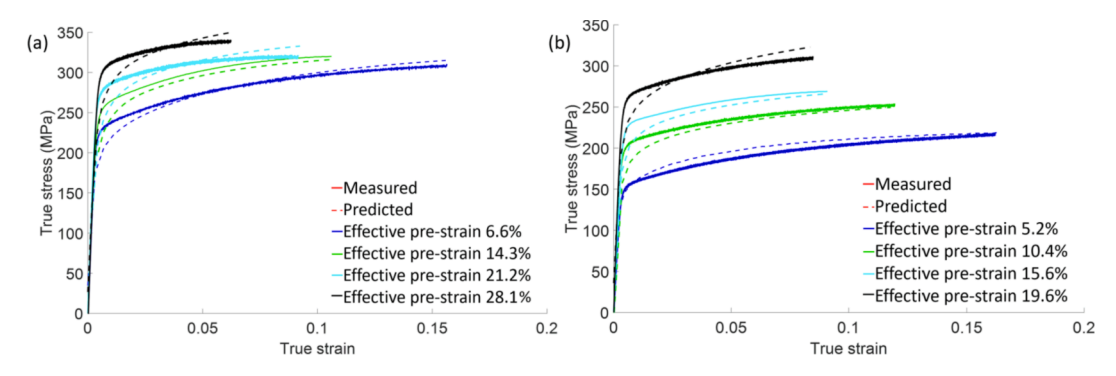


Fig. 9. As measured and predicted tensile curves for specimens pre-strained in (a) biaxial, and (b) plane-strain tension. The percent of pre-strain represents the effective strain imposed by the Marciniak Test. The levels of effective strain correspond to 25%, 50%, 75%, and 95% of failure.

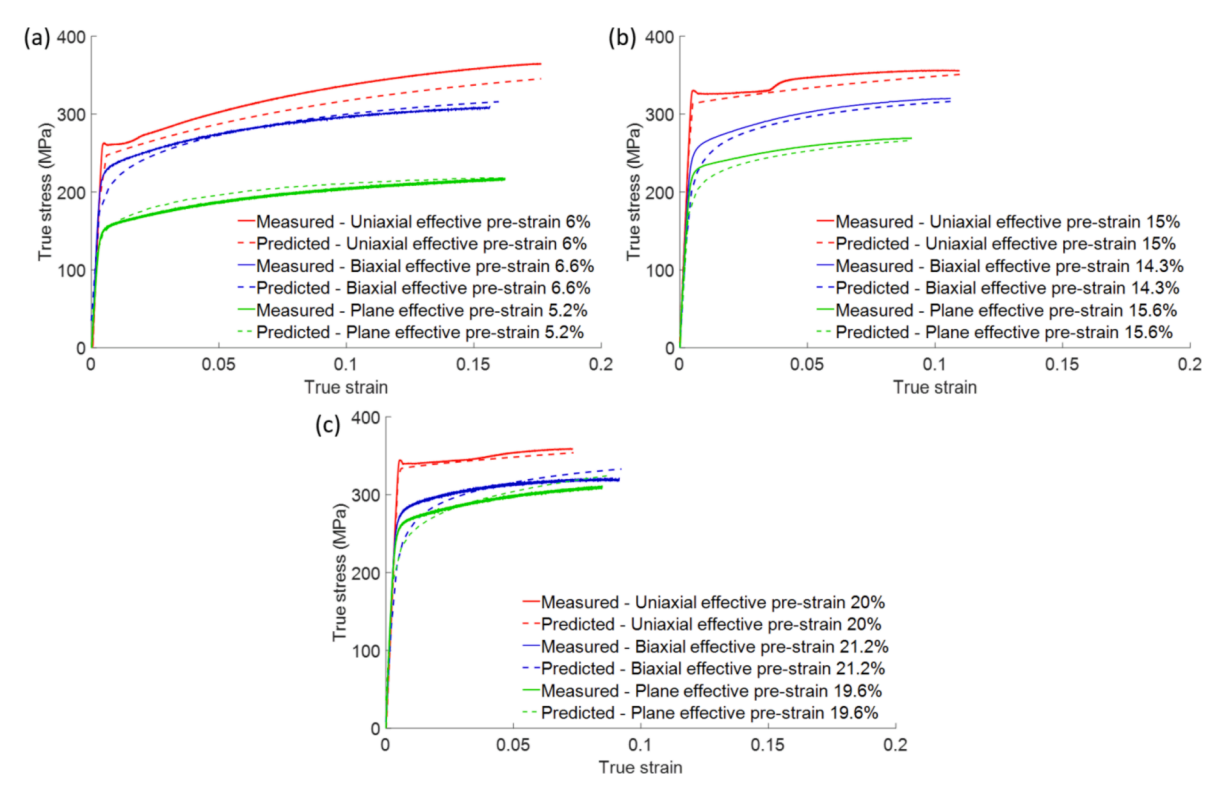


Fig. 10. As-measured and predicted uniaxial work hardening comparison after pre-straining to different levels of uniaxial, biaxial, and plane-strain tension.

The predictions for biaxial-to-uniaxial and plane-strain-to-uniaxial follow a slower elasto-plastic transition than the measured data and the yield strength is underpredicted. In the model, the residual stress in the material from the pre-strain deformation was effectively frozen at that level for subsequent uniaxial tension pulls. As described earlier, the inter-granular stresses in EPSC are a consequence of the interaction between individual grains and the averaged polycrystalline response. Therefore, these stresses are approximations of true local grain-to-grain interactions. Experimentally, the uniaxial tension specimens were waterjet cut from the pre-strained biaxial and plane-strain tension Marciniak sheets, which could allow some stress relaxation. For the current analysis, the amount of residual stress was not measured; however, it could potentially be measured using XRD analysis to test this hypothesis.

Upon reaching yield point the uniaxial-to-uniaxial specimens demonstrated a yield point phenomenon (YPP); the stress drops immediately after yield, and there is a period of hardening stagnation, the length of which correlates with the pre-strain level. However, the phenomenon is not reflected for initial uniaxial, biaxial-to-uniaxial, and plane-strain-to-uniaxial tension deformations. The biaxial-to-uniaxial and plane-strain-to-uniaxial specimens had a significant processing time gap between the pre-strain and subsequent pulls; hence the uniaxial tension pre-strained specimens were also rested for ~ 24 hrs. to determine whether this affected the response; they still showed YPP under subsequent pulls. As hypothesized by Cottrell, dislocations attract solute atoms; if solute atoms are allowed to migrate and form local atmospheres around the dislocation, they become pinned, leading to higher yield stress. At yield, the dislocations break free of the atmospheres, leading to lower subsequent stress required for further deformation (Cottrell and Bilby, 1949). Since the effect is absent in the initial uniaxial tension curves, it is assumed that as-received AA6016-T4 has the dislocations already broken away from the solute atmospheres during the manufacturing process. However, only uniaxial pre-strain appears to recombine them so that they require breakaway stress for subsequent uniaxial pulls - possibly relating to the particular slip characteristics during uniaxial tension while different slip systems activate upon a

strain-path-change. There is a possibility that a mechanism other than Cottrell's theory causes YPP for these experiments, which is a subject for future studies.

Fig. 11 shows the slip system activity ( $\sum \rho^{tot}$  as defined in Eq. (11)) from the EPSC model for pre-strain deformation under all three strain paths. The slip systems are grouped per plane. Consideration of the predicted activity on different slip systems indicates a significant difference between the three pre-strain modes. It may help explain the different levels of cross-slip between slip systems that lead to different hardening rates. The slip planes with similar activity could have a higher probability of cross-slip and the strain paths that have relatively more slip planes with similar activity could consequently have relatively higher cross-slip. This is most notable for biaxial and uniaxial tension, which both have two pairs of planes with similar activity. The biaxial deformation is predicted as the most homogeneous.

Finally, the backstress component was excluded from the EPSC model while keeping other parameters the same and the results were then compared to the initial predictions with backstress development; both cases are compared with measured data (for the  $\sim 20\%$  effective pre-strain case) in Fig. 12. The trends for all other pre-strain levels were similar. It can be observed that the flow stress levels for the subsequent uniaxial tension from EPSC with no backstress development are about 15% below those from EPSC with backstress development, and from the experimentally measured curves, at high strain levels. As stated earlier, a sharp elastic to plastic transition and linear hardening for uniaxial prestrain is a result of increased dislocation density on already activated slip systems from pre-straining. The effect is also evident for EPSC results with no backstress development. Furthermore, the EPSC results help to explain post-yield hardening in the uniaxially pre-strained samples compared with the other two cases. A uniaxially pre-strained sample has developed backstress that counteracts uniaxial deformation; upon reloading, the backstress is already in place to add with the dislocation flow stress, resulting in little difference in hardening rate after yield between the case with and without backstress. For the other pre-strained samples, the backstress was developed to counter deformation in other directions; when pulled in uniaxial tension the backstress does not

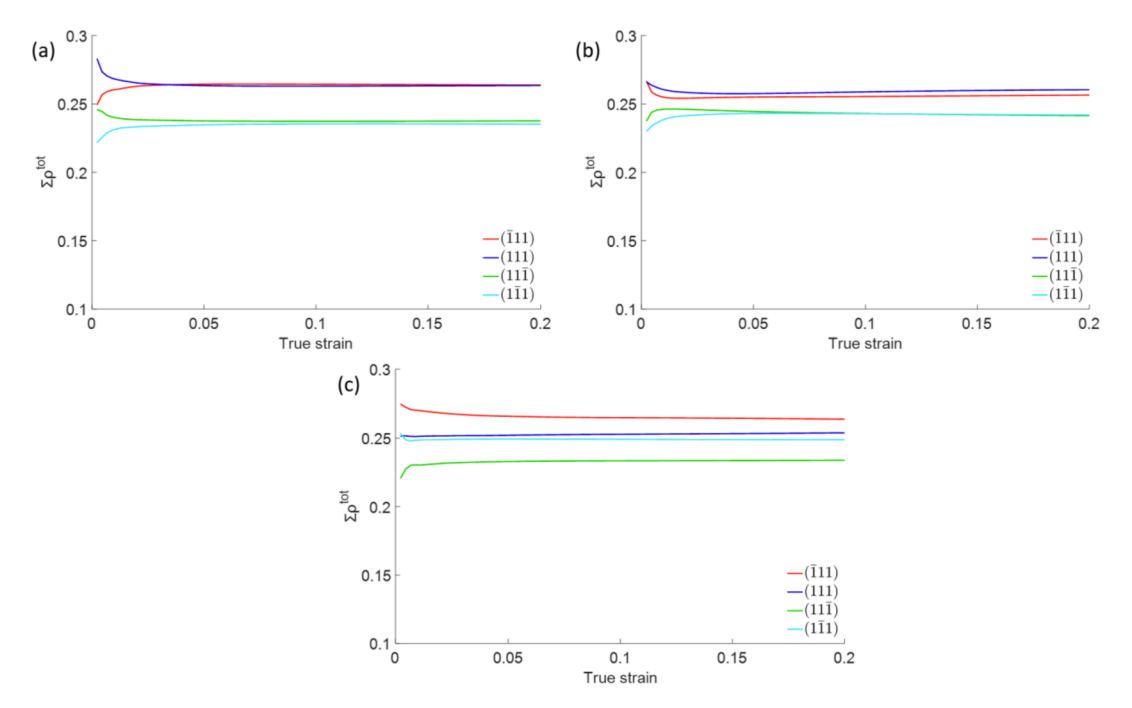


Fig. 11. Slip system activity ( $\sum \rho^{tot}$  is the total dislocation density for a given slip plane, as described in Eq. (11)), extracted from the model for the pre-strain deformation response of (a) uniaxial, (b) biaxial, and (c) plane-strain tension.

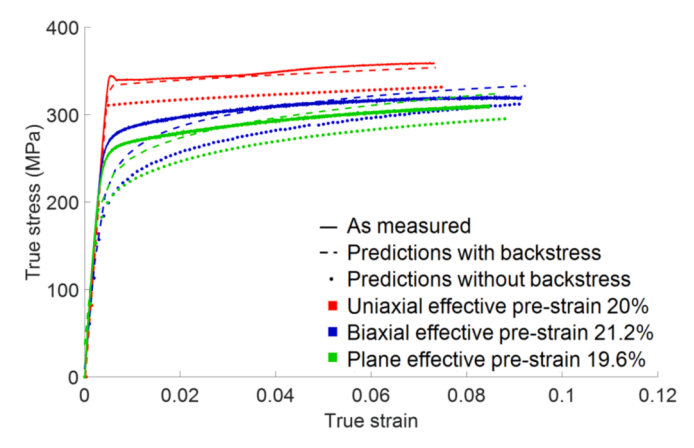


Fig. 12. EPSC predictions with and without backstresses taken into account, compared to the measured work hardening behavior post strain path change. Measured data is represented by a continuous curve, ESPC predictions with backstress are represented by dashed curve and predictions without backstress are represented by a dotted curve. Colors representing the corresponding strain paths are shown in the legend.

immediately contribute to early hardening, but builds up over the first 1% strain, or so. This leads to a more gradual transition from the elastic to the plastic portion of the curve. In all cases, the backstress builds up early in the deformation, in agreement with the literature stating that kinematic hardening dominates during the first  $\sim\!2\%$  of deformation (Ashby, 1970).

The current study focused on comparing the plastic behavior of AA6016-T4 using the yield curves. Often, an alternative validation such as Lankford parameter is employed which can capture a relatively higher contrast of comparison in response to a strong texture evolution due to plastic deformation. This was investigated by measuring the R-values for uniaxial and biaxial pre-strain as shown in Table 7. Table 7 also compares the yield strengths for both the pre-strains. An increase of 64% in the R-value of biaxial pre-strain with respect to uniaxial pre-strain was observed, in contrast to an increase of 32% in the yield

**Table 7**Comparison between the Lankford coefficient and post pre-straining yield strength of uniaxial and biaxial pre-strains paths.

Effective Pre-strain	Post-uniaxial strain (Avg. Green -lagrangian strain)	R value (Lankford coefficient)	Post pre-strain Yield strength (MPa)
Uniaxial	0.05	0.477	330
Biaxial 15%	0.0468	0.77	250

strength of uniaxial pre-strain with respect to biaxial pre-strain. Hence, while the R-value does present a bigger contrast than the yield curves for different pre-strains, it is not an order of magnitude higher. Furthermore, the ability of the same model to calculate R-values of a similar AA6022-T4 alloy has been assessed successfully in previously published studies (Barrett and Knezevic, 2019; Feng et al., 2020). Therefore, a comparison of yield curves for multi-strain path deformation is sufficient for AA6016-T4.

### 4. Conclusions

An EPSC model, with the inclusion of backstresses, is employed to predict the pre-straining of AA6016-t4 sheet material under uniaxial, biaxial, and plane-strain tension, along with the subsequent deformation response under uniaxial tension. The EPSC model correctly captures the effects of texture, being able to distinguish the subtle differences in response for RD, TD, and ND direction under uniaxial tension. Furthermore, the EPSC model was able to correctly predict the uniaxial response after first pre-straining in biaxial, plane-strain, and uniaxial tension. The model correctly predicted the highest flow stress in uniaxially pre-strained material, followed by lower stresses in the biaxially and plane-strain tension deformed materials, respectively. The model slightly overpredicts the hardening rate for materials pre-strained to high levels under biaxial or plane-strain tension. This is likely due to some incipient localization in these samples during the pre-strain operation (as confirmed by the DIC measurements).

Importantly, the model also captures the rapid buildup of backstress

in the uniaxially pre-strained specimens; conversely, it correctly predicts the slower buildup of backstress in the other pre-strained specimens and the smoother transition between the elastic and plastic regions. At higher strain levels the backstress accounted for around 15% of the total flow stress in all pre-strain cases.

The backstress builds up in the early stages of plastic deformation, consistent with the current understanding of kinematic hardening dominating early deformation, and isotropic hardening dominating at higher strains. This picture also agrees with an HREBSD-measured linear increase in GND density (associated with kinematic hardening), compared with a quadratic increase in the SSD (associated with isotropic hardening) predicted by the EPSC model, both of which are in line with expectations. The initial total dislocation density assumed by the EPSC model is slightly below measured GND density; hence some work to improve the connection between measured and calibrated dislocation density (including incorporation of GND content) will occur in the future. To this end, the EPSC model will be advanced to consider second moments of stress and spin tensors in order to calculate GNDs as recently formulated in VPSC (Zecevic et al., 2017).

# **Declaration of Competing Interest**

The authors declare that they have no known competing financial interests or personal relationships that could have appeared to influence the work reported in this paper.

# Acknowledgments

The work presented in this paper was supported by National Science Foundation grant number CMMI-1926662 (BYU) and CMMI-1926677 (UNH).

# References

- Al-Harbi, H.F., Knezevic, M., Kalidindi, S.R., 2010. Spectral approaches for the fast computation of yield surfaces and first-order plastic property closures for polycrystalline materials with cubic-triclinic textures. Retrieved from Comput. Mater. Cont. 15 (2), 153–172. https://www.scopus.com/inward/record.uri?eid=2-s2.0-77954195006&partnerID=40&md5=457b8ec9363658379ef586ea60496567.
- ARAMIS 3D Digital Image Correlation Strain & 3D Deformation. (2011): Trillion Optical Test System.
- Ashby, M.F., 1970. The deformation of plastically non-homogeneous materials. Phil. Mag. 21 (170), 399–424.
- Barrett, T.J., Knezevic, M., 2019. Deep drawing simulations using the finite element method embedding a multi-level crystal plasticity constitutive law: Experimental verification and sensitivity analysis. Comput. Methods Appl. Mech. Eng. 354, 245–270. https://doi.org/10.1016/j.cma.2019.05.035.
- Beyerlein, I.J., Tomé, C.N., 2008. A dislocation-based constitutive law for pure Zr including temperature effects. Retrieved from Int. J. Plast. 24 (5), 867–895. http:// www.sciencedirect.com/science/article/pii/S074964190700109X.
- Bouaziz, O., Moon, J., Kim, H.S., Estrin, Y., 2021. Isotropic and kinematic hardening of a high entropy alloy. Scr. Mater. 191, 107–110. https://doi.org/10.1016/j. scriptamat.2020.09.022.
- Brewer, L.N., Field, D.P., Merriman, C.C., 2009. Mapping and assessing plastic deformation using EBSD. In: Schwartz, A.J., Kumar, M., Adams, B.L., Field, D.P. (Eds.), Electron Backscatter Diffraction in Materials Science, 2nd Ed. Springer, pp. 251–262.
- BYU. (2015). OpenXY (Version 1.0): github.com. Retrieved from https://github.com/BYU-MicrostructureOfMaterials/OpenXY.git.
- Chen, X., Jiao, R., Kim, K., 2003. Simulation of ratcheting strain to a high number of cycles under biaxial loading. Int. J. Solids Struct. 40 (26), 7449–7461.
- Chen, X., Peng, Y., Chen, C., Li, J., Wang, K., Wang, T., 2019. Mechanical behavior and texture evolution of aluminum alloys subjected to strain path changes: Experiments and modeling. Mater. Sci. Eng. A 757, 32–41.
- Cheng, J., Green, D.E., Golovashchenko, S.F., 2017. Formability enhancement of DP600 steel sheets in electro-hydraulic die forming. J. Mater. Process. Technol. 244, 178–189.
- Cottrell, A.H., Bilby, B.A., 1949. Dislocation theory of yielding and strain ageing of iron. Proc. Phys. Soc. A 62 (1), 49–62.
- Dequiedt, J., Denoual, C., Madec, R., 2015. Heterogeneous deformation in ductile FCC single crystals in biaxial stretching: the influence of slip system interactions. J. Mech. Phys. Solids 83, 301–318.
- Devincre, B., Kubin, L., Hoc, T., 2006. Physical analyses of crystal plasticity by DD simulations. Scr. Mater. 54 (5), 741–746. https://doi.org/10.1016/j.scriptamat.2005.10.066.

- Ebobisse, F., Neff, P., 2010. Existence and uniqueness for rate-independent infinitesimal gradient plasticity with isotropic hardening and plastic spin. Mathemat. Mech. Solids 15 (6), 691–703.
- Eghtesad, A., Barrett, T.J., Germaschewski, K., Lebensohn, R.A., McCabe, R.J., Knezevic, M., 2018. OpenMP and MPI implementations of an elasto-viscoplastic fast Fourier transform-based micromechanical solver for fast crystal plasticity modeling. Adv. Eng. Softw. 126, 46–60. https://doi.org/10.1016/j.advengsoft.2018.09.010.
- El-Madhoun, Y., Mohamed, A., Bassim, M., 2003. Cyclic stress-strain response and dislocation structures in polycrystalline aluminum. Mater. Sci. Eng., A 359 (1–2), 220–227.
- Eshelby, J.D., 1957. The determination of the elastic field of an ellipsoidal inclusion, and related problems. Proc R. Soc. Lond. A 241, 376–396.
- Feng, Z., Yoon, S.-Y., Choi, J.-H., Barrett, T.J., Zecevic, M., Barlat, F., Knezevic, M., 2020. A comparative study between elasto-plastic self-consistent crystal plasticity and anisotropic yield function with distortional hardening formulations for sheet metal forming. Mech. Mater. 148, 103422 https://doi.org/10.1016/j. mechant 2020 103422
- Ghorbanpour, S., Zecevic, M., Kumar, A., Jahedi, M., Bicknell, J., Jorgensen, L., Beyerlein, I.J., Knezevic, M., 2017. A crystal plasticity model incorporating the effects of precipitates in superalloys: application to tensile, compressive, and cyclic deformation of Inconel 718. Int. J. Plast. 99, 162–185.
- Goh, C.-H., Neu, R.W., McDowell, D.L., 2003. Crystallographic plasticity in fretting of Ti-6AL-4V. Int. J. Plast. 19 (10), 1627–1650.
- Graf, A., Hosford, W., 1994. The influence of strain-path changes on forming limit diagrams of Al 6111 T4. Int. J. Mech. Sci. 36 (10), 897–910.
- Graf, A.F., Hosford, W.F., 1993. Calculations of forming limit. Metall. Trans. A 24 (11), 2497–2501.
- Hoc, T., Devincre, B., & Kubin, L. (2004). Deformation stage I of FCC crystals: Constitutive modelling. Paper presented at the 25 th Riso International Symposium on Materials Science 2004.
- Jiang, J., Britton, T., Wilkinson, A., 2013. Evolution of dislocation density distributions in copper during tensile deformation. Acta Mater. 61 (19), 7227–7239.
- Khadyko, M., Dumoulin, S., Cailletaud, G., Hopperstad, O.S., 2016. Latent hardening and plastic anisotropy evolution in AA6060 aluminium alloy. Int. J. Plast. 76, 51–74. https://doi.org/10.1016/j.ijplas.2015.07.010.
- Kitayama, K., Tomé, C.N., Rauch, E.F., Gracio, J.J., Barlat, F., 2013. A crystallographic dislocation model for describing hardening of polycrystals during strain path changes. Application to low carbon steels. Int. J. Plast. 46, 54–69. https://doi.org/ 10.1016/j.ijplas.2012.09.004.
- Knezevic, M., Al-Harbi, H.F., Kalidindi, S.R., 2009. Crystal plasticity simulations using discrete Fourier transforms. Acta Mater. 57 (6), 1777–1784. https://doi.org/ 10.1016/j.actamat.2008.12.017.
- Knezevic, M., Kalidindi, S.R., Fullwood, D., 2008. Computationally efficient database and spectral interpolation for fully plastic Taylor-type crystal plasticity calculations of face-centered cubic polycrystals. Int. J. Plast. 24 (7), 1264–1276. https://doi.org/ 10.1016/j.ijnlas.2007.12.002.
- Knezevic, M., Savage, D.J., 2014. A high-performance computational framework for fast crystal plasticity simulations. Comput. Mater. Sci. 83, 101–106. https://doi.org/ 10.1016/j.commatsci.2013.11.012.
- Knockaert, R., Chastel, Y., Massoni, E., 2000. Rate-independent crystalline and polycrystalline plasticity, application to FCC materials. Int. J. Plast. 16 (2), 179–198. https://doi.org/10.1016/S0749-6419(99)00071-6.
- Kocks, U.F., Franciosi, P., Kawai, M., 1991. A forest model of latent hardening and its application to polycrystal deformations. Text. Microstruct. 14, 1103–1114. https://doi.org/10.1155/tsm.14-18.1103.
- Laukonis, J.V., Ghosh, A.K., 1978. Effects of strain path changes on the formability of sheet metals. Metall. Mater. Trans. A 9 (12), 1849–1856.
- Lavrentev, F.F., 1980. The type of dislocation interaction as the factor determining work hardening. Retrieved from Mater. Sci. Eng. 46 (2), 191–208. http://www.science direct.com/science/article/pii/0025541680901755.
- Li, S., Hoferlin, E., Bael, A.V., Houtte, P.V., Teodosiu, C., 2003. Finite element modeling of plastic anisotropy induced by texture and strain-path change. Int. J. Plast. 19 (5), 647–674. https://doi.org/10.1016/S0749-6419(01)00079-1.
- Lipinski, P., Berveiller, M., 1989. Elastoplasticity of micro-inhomogeneous metals at large strains. Int. J. Plast. 5 (2), 149–172. https://doi.org/10.1016/0749-6419(89) 90027-2.
- Liu, B., Raabe, D., Roters, F., Eisenlohr, P., Lebensohn, R.A., 2010. Comparison of finite element and fast Fourier transform crystal plasticity solvers for texture prediction. Modell. Simul. Mater. Sci. Eng. 18 (8), 085005 https://doi.org/10.1088/0965-0393/ 18/8/085005.
- Lloyd, D., Sang, H., 1979. The influence of strain path on subsequent mechanical properties—Orthogonal tensile paths. Metall. Trans. A 10 (11), 1767–1772.
- Mecking, H., Kocks, U.F., 1981. Kinetics of flow and strain-hardening. Acta Metall. Mater. 29 (11), 1865–1875.
- Mirzaei, M., Roshan, M.R., Jenabali Jahromi, S.A., 2015. Microstructure and mechanical properties relation in cold rolled Al 2024 alloy determined by X-ray line profile analysis. Mater. Sci. Eng., A 620, 44–49. https://doi.org/10.1016/j. msea.2014.09.110.
- Moan, G., & Embury, J. (1979). A study of the bauschinger effect in Al Cu alloys. *Acta Metallurgica*, 27(5), 903-914.
- Nagtegaal, J.C., Veldpaus, F.E., 1984. On the implementation of finite strain plasticity equations in a numerical model. Numer. Methods Ind. Form. Process. 351–371.
- Neil, C.J., Wollmershauser, J.A., Clausen, B., Tomé, C.N., Agnew, S.R., 2010. Modeling lattice strain evolution at finite strains and experimental verification for copper and stainless steel using in situ neutron diffraction. Int. J. Plast. 26 (12), 1772–1791. https://doi.org/10.1016/j.ijplas.2010.03.005.

- Nugmanov, D., Knezevic, M., Zecevic, M., Sitdikov, O., Markushev, M., Beyerlein, I.J., 2018. Origin of plastic anisotropy in (ultra)-fine-grained Mg–Zn–Zr alloy processed by isothermal multi-step forging and rolling: Experiments and modeling. Mater. Sci. Eng., A 713, 81–93. https://doi.org/10.1016/j.msea.2017.12.045.
- OIM 6.0. (2010): EDAX-TSL.
- Raabe, D., Roters, F., 2004. Using texture components in crystal plasticity finite element simulations. Retrieved from Int. J. Plast. 20 (3), 339–361. http://www.sciencedirect. com/science/article/B6TWX-49DFBPM-6/2/21cdd5c76262041b9b55325d7195 baa4.
- Rovinelli, A., Proudhon, H., Lebensohn, R.A., Sangid, M.D., 2020. Assessing the reliability of fast Fourier transform-based crystal plasticity simulations of a polycrystalline material near a crack tip. Int. J. Solids Struct. 184, 153–166. https:// doi.org/10.1016/j.ijsolstr.2019.02.024.
- Ruggles, T., Fullwood, D., 2013. Estimations of bulk geometrically necessary dislocation density using high resolution EBSD. Ultramicroscopy 133, 8–15.
- Savage, D.J., Knezevic, M., 2015. Computer implementations of iterative and noniterative crystal plasticity solvers on high performance graphics hardware. Comput. Mech. 56 (4), 677–690. https://doi.org/10.1007/s00466-015-1194-6.
- Segurado, J., LLorca, J., 2010. Discrete dislocation dynamics analysis of the effect of lattice orientation on void growth in single crystals. Int. J. Plast. 26 (6), 806–819.
- Stoltz, R., & Pelloux, R. (1974). Cyclic deformation and bauschinger effect in Al Cu Mg alloys. Scripta Metallurgica, 8(3), 269-275.
- Stoltz, R., Pelloux, R., 1976. The Bauschinger effect in precipitation strengthened aluminum alloys. Metall. Trans. A 7 (8), 1295–1306.
- Taylor, G.I., 1938. Plastic strain in metals. J. Inst. Met. 62, 307-324.
- Teodosiu, C., Raphanel, J.L., 1991. Finite element simulations of large elastoplastic deformations of multicrystals. In: Proceedings of the International Seminar MECAMAT91, pp. 153–168.
- Turner, P.A., Tomé, C.N., 1994. A study of residual stresses in Zircaloy-2 with rod texture. Retrieved from Acta Metall. Mater. 42 (12), 4143–4153. http://www.sciencedirect.com/science/article/pii/0956715194901910.
- Wen, W., Borodachenkova, M., Tomé, C.N., Vincze, G., Rauch, E.F., Barlat, F., Grácio, J. J., 2015. Mechanical behavior of Mg subjected to strain path changes: Experiments and modeling. Int. J. Plast. 73, 171–183. https://doi.org/10.1016/j.iiplas.2014.10.009.

- Wollmershauser, J.A., Clausen, B., Agnew, S.R., 2012. A slip system-based kinematic hardening model application to in situ neutron diffraction of cyclic deformation of austenitic stainless steel. Int. J. Fatigue 36 (1), 181–193. https://doi.org/10.1016/j. iifatigue 2011 07 008
- Woo, W., Ungár, T., Feng, Z., Kenik, E., Clausen, B., 2010. X-ray and neutron diffraction measurements of dislocation density and subgrain size in a friction-stir-welded aluminum alloy. Metall. Mater. Trans. A 41 (5), 1210–1216.
- Wright, S.I., Suzuki, S., Nowell, M.M., 2016. In situ EBSD observations of the evolution in crystallographic orientation with deformation. JOM 68 (11), 2730–2736.
- Zecevic, M., Knezevic, M., 2018. Latent hardening within the elasto-plastic self-consistent polycrystal homogenization to enable the prediction of anisotropy of AA6022-T4 sheets. Int. J. Plast. 105, 141–163. https://doi.org/10.1016/j.iiplas.2018.02.007.
- Zecevic, M., & Knezevic, M. (2019). An implicit formulation of the elasto-plastic self-consistent polycrystal plasticity model and its implementation in implicit finite elements. *Mechanics of Materials*, 136, 103065.
- Zecevic, M., Knezevic, M., Beyerlein, I.J., Tomé, C.N., 2015. An elasto-plastic selfconsistent model with hardening based on dislocation density, twinning an detwinning: Application to strain path changes in HCP metals. Mater. Sci. Eng. A 638, 262-274.
- Zecevic, M., Korkolis, Y.P., Kuwabara, T., Knezevic, M., 2016. Dual-phase steel sheets under cyclic tension—compression to large strains: Experiments and crystal plasticity modeling. J. Mech. Phys. Solids 96, 65–87. https://doi.org/10.1016/j. imps.2016.07.003.
- Zecevic, M., Pantleon, W., Lebensohn, R.A., McCabe, R.J., Knezevic, M., 2017. Predicting intragranular misorientation distributions in polycrystalline metals using the viscoplastic self-consistent formulation. Acta Mater. 140, 398–410.
- Zecevic, M., Upadhyay, M.V., Polatidis, E., Panzner, T., Van Swygenhoven, H., Knezevic, M., 2019. A crystallographic extension to the Olson-Cohen model for predicting strain path dependence of martensitic transformation. Acta Mater. 166, 386–401. https://doi.org/10.1016/j.actamat.2018.12.060.
- Zheng, J.-H., Pruncu, C., Zhang, K., Zheng, K., Jiang, J., 2021. Quantifying geometrically necessary dislocation density during hot deformation in AA6082 Al alloy. Mater. Sci. Eng., A 814, 141158. https://doi.org/10.1016/j.msea.2021.141158.